

Scalable Fabrication of Height-Variable Microstructures with a Revised Wetting Model

Prabuddha De Saram, Nam-Trung Nguyen,* and Navid Kashaninejad*

Varying the height of microstructures is crucial for tuning surface properties such as wettability, adhesion, and optical characteristics, which are essential in applications from microfluidics to biosensing. However, conventional techniques for fabricating height-variable microstructures are often costly and labor-intensive, involving multiple intricate steps. Herein, an innovative, rapid, and cost-effective approach using CO₂ laser-machined poly (methyl methacrylate) (PMMA) molds to produce height-variable microstructures in polydimethylsiloxane (PDMS) is introduced. The method leverages varying laser fluence to precisely control feature depth on PMMA substrates, creating high-fidelity negative molds without requiring surface chemical modifications. The applicability of Cassie–Baxter and Wenzel equations to height-variable microstructures is systematically investigated. To this aim, six sharkskin surfaces with controlled height gradients are fabricated and their wettability behavior is studied. Results show pronounced anisotropic hydrophobicity, with variations in contact angles and sliding angles in one direction depending on height-induced curvature effects. These conclusions establish that classical wetting models neglect to consider fully the effect of height gradients on droplet behavior. By proposing a modified equation that includes the variable contact plane curvature according to heights, the prediction validity of wettability onto structured surfaces is enhanced. These insights provide a fundamental understanding of wetting behavior on height-variable microstructures.

which can be produced using any micro-manufacturing techniques capable of forming 3D structures and subsequently casting polymer replicates with the mold.^[1] While photolithography remains a widely used method for mold manufacturing, newer techniques have emerged to enhance mold fabrication efficiency and complexity.^[2] Among these, 3D printing offers versatile capabilities for creating molds with diverse microstructure geometries.^[3,4] Direct laser machining, another promising technique, is well-documented in soft lithography for mold fabrication.^[5] However, almost all studies with laser micromachining to date have focused on 2.5D geometries with fixed structural heights.^[6]


Direct laser micromachining offers several advantages, such as contact-free operation, reduced processing times, enhanced design flexibility, good resolution, and no requirement for postprocessing.^[7] CO₂ lasers, in particular, are noted for their cost-effectiveness and ease of use, requiring less specialized technical knowledge.^[8] The use of CO₂ laser micromachining for directly fabricating microstructures, particularly microchannels, in polymethyl methacrylate (PMMA) has been extensively studied.^[9,10] CO₂ lasers emit a beam with a Gaussian intensity profile, which results in a Gaussian-shaped ablation profile on PMMA. This ablated profile can be directly utilized to create microchannels. The depth, width, shape, and surface properties of the machined features are influenced by laser parameters such as power, speed, number of passes, focus, and the material properties of PMMA. Numerous studies have explored the relationships between these parameters and their optimization to achieve the desired outcomes.^[10–12]

Variable-height microstructures, such as micropillars and ribs, have proven valuable in various microfluidic studies, including cell mechanobiology, fluid manipulation, and surface property modulation. These structures are crucial for advancements in biosensing and electrode development.^[13–16] For instance, varying the height of micropillars can modulate extracellular matrix stiffness, allowing researchers to investigate cell mechanotransduction processes.^[17] The challenge of fabricating structures with varying heights remains a significant barrier for widespread applications of height-varying structures. Traditional photolithography involves complex steps, even for creating just two distinct height levels.^[13] Although rapid prototyping methods

1. Introduction

Soft lithography is a well-established technique for fabricating polymeric microstructures, especially in microfluidic applications. This method typically involves creating a negative mold,

P. De Saram, N.-T. Nguyen, N. Kashaninejad
Queensland Micro- and Nanotechnology Centre
Nathan Campus
Griffith University
170 Kessels Road, Brisbane QLD 4111, Australia
E-mail: nam-trung.nguyen@griffith.edu.au;
n.kashaninejad@griffith.edu.au

 The ORCID identification number(s) for the author(s) of this article can be found under <https://doi.org/10.1002/adem.202500234>.

© 2025 The Author(s). Advanced Engineering Materials published by Wiley-VCH GmbH. This is an open access article under the terms of the Creative Commons Attribution-NonCommercial-NoDerivs License, which permits use and distribution in any medium, provided the original work is properly cited, the use is non-commercial and no modifications or adaptations are made.

DOI: 10.1002/adem.202500234

like micro-stereolithography, two-photon lithography, and localized electrochemical deposition can directly fabricate these microstructures, they require costly and sophisticated equipment.^[18,19]

Sharkskin is renowned for its unique microstructured surface, which offers remarkable properties such as reduced drag, anti-fouling, and antibacterial effects.^[20] These attributes stem from its unique riblet structures with varying heights,^[21] a feature often overlooked in artificial replicas. Bhushan et al. extensively studied the effect of riblets and sharkskin patterns on fluid drag reduction on surfaces.^[22,23] Riblets can reduce the fluid drag by controlling the turbulent vortices leading to less momentum transfer and shear stress, reducing the drag. Primarily, riblets lift the vortices above the surface, pinning them to the riblet tips. This reduces the shear stress caused by the interaction of vortices with the large surface area to riblet tips. Also, riblets can confine the streamwise vortices within the riblets, reducing their ability to interact with each other and the outer turbulent boundary layer, which could cause further energy loss.^[23,24] Mechanisms of drag reduction by sharkskin structures are comprehensively reviewed elsewhere.^[25] Except for a few, most of these studies have not captured the height-varying nature of natural sharkskin structures. Bixler et al. studied the relationship between fluid drag and riblet parameters such as height, inter riblet space, and shape showing the changes of drag with riblet height.^[24,26] However, they have not varied the riblet height within the substrates. Using two-photon lithography, Cui et al. developed a sharkskin-like surface with three riblet height levels.^[14] While their structure demonstrated enhanced drag reduction and antifouling compared to uniform-height designs, it did not fully capture the natural height variability pattern of sharkskin.

Manipulation of surface wettability is a widely used method to control droplet transportation on surfaces.^[27] Riblet-like structures can induce directional variability in contact angles, while riblet geometry can influence droplet sliding resistance on surfaces.^[28] When riblets are sufficiently high, fluids sit on the riblets in the Cassie–Baxter (CB) state. In this state, the microstructures on the surface create air pockets beneath the liquid, reducing the solid–liquid contact area, and making the surface hydrophobic. Taller structures can induce higher contact angles by trapping more air beneath the droplet. Thus, by adjusting the structural height, it should be possible to manipulate the contact angle on the same substrate.^[29] Some studies have highlighted the impact of height variability on drag and droplet dynamics,^[21,30,31] but a comprehensive understanding of how height variations affect surface properties remains limited, as fabricating height-varying riblet structures using conventional processes is challenging.

In this study, we seek to fill this gap by applying CO₂ laser milling to fabricate sharkskin-type riblet constructs with height gradients, thereby facilitating a systematic evaluation of the breakdown of classical wetting models in situations of height change. Sharkskin-like surfaces are particularly interesting due to their height gradients, which introduce anisotropic wettability effects. Unlike previous studies focusing only on applications, the current work aims to use these structures as a controlled model system for the fundamental assessment of wettability on height-variable surfaces. Eight different heights were fabricated from PMMA molds replicated in PDMS, and the effects of height gradients on the contact angle, sliding angle, and contact angle hysteresis were analyzed systematically. The

experimental data showed significant deviation from CB and Wenzel’s predictions, revealing the necessity for a modified theoretical framework. By including height-dependent contact plane curvature correction, we propose an improved model that offers enhanced predictions of wettability on structured surfaces.

2. Experimental Section

2.1. Surface Fabrication

We fabricated six distinct sharkskin-like surfaces with varying height gradients using replicating techniques with PMMA molds. These molds were produced using a Trotec Speedy 300 CO₂ laser cutting machine. The machine allows for the adjustment of laser power and speed coded as colors of the design, enabling control over the height gradients with a single machining pass. The CO₂ laser operates at a wavelength of 10.6 μm and delivers a maximum power of 90 W.

To create structures with varying heights, we varied the laser power in steps of 0.2, 0.4, 0.6, 0.8, and 1%, starting from an initial power of 4.6%. The laser scanning speed was kept constant at 4% of the machine’s maximum speed, which is 3.55 m s^{−1}. For comparison, a control surface with a uniform height was fabricated using a fixed laser power of 6.2%. The six surfaces were designated as G0 (Gradient 0) through G5, with G0 representing the control surface (no laser power variation) and G5 corresponding to the highest variation (1% at each height level). The riblet geometries were oriented such that their longer axis was parallel to the laser scanning direction. The design width of the riblets was set at 130 μm. The machine software automatically performed four overlapping laser passes with offsets of 30, 20, and 30 μm. The scanning was executed at a resolution of 1,000 dpi. The final structured surfaces were then replicated using a PDMS mixture (prepolymer and cross-linker) in a 10:1 ratio. The PDMS was cast into the molds and cured in a vacuum oven at 80 °C for 3 h.

2.2. Ablation Model

The theoretical modeling of laser ablation is well-documented in the literature.^[32,33] In the context of polymer laser machining, certain factors, such as heat conduction, play a less critical role than metals. Prakash et al. have extensively studied laser ablation depths in PMMA and proposed a simplified model based on energy balance to estimate the ablation profile for a continuous wave laser beam with a Gaussian intensity profile, Equation (1).^[8,34] This model focuses on the balance between the material vaporization energy and the energy supplied by the laser without accounting for factors such as molten material ejection, cooling rates, or heat conductivity. Despite these limitations, experimental results reported by Prakash et al. demonstrate that this model can predict machining depths with over 90% accuracy in PMMA.^[35]

$$z(y) = \frac{\alpha(\theta)}{\rho(c_p \Delta T + H_L)} \cdot \sqrt{\frac{2}{\pi w^2}} \cdot \frac{P}{U} \cdot e^{-\frac{2y^2}{w^2}} \quad (1)$$

where z is the depth of each y location across the machined profile, ρ , c_p , and H_L are density, specific heat capacity, and

the latent heat of vaporization of the material, respectively. ΔT indicates the temperature rise from the ambient to the degradation point. The radius w of the laser spot is defined as where the laser intensity drops to $1/e^2$ of the maximum intensity. P and U refer to the power and scan speed of the laser, respectively. The absorptivity $\alpha(\theta)$ of the laser energy from the material surface is influenced by the angle θ at which the laser impinges on the surface. For the first pass, $\theta = 0$, from the second pass onward, $\tan \theta = \frac{dz(y)}{dy}$ of the previous pass. As the laser no longer focuses on the machining surface from the second pass onward, the laser spot diameter changes. Additionally, the heat-affected zone can alter the material properties and absorptivity.^[35]

2.3. Surface Characterization

The 2D surface features of the fabricated surfaces were characterized using an inverted brightfield microscope (Olympus IX73, Olympus Corporation, Tokyo, Japan). Structural heights and surface roughness measurements of the final replicated designs and molds were measured using a 3D laser scanning microscope (Olympus LEXT OLS5100, Olympus Corporation, Tokyo, Japan) equipped with a 10x-objective lens. A scanning electron microscope (SEM) (Thermo Fisher Scientific Apreo 2, Thermo Fisher Scientific, Waltham, MA, USA) was employed to observe microfeatures.

2.4. Surface Wettability Characterization

Water contact angle (CA) and sliding angle measurements were conducted using an optical tensiometer (Biolin Scientific ThetaFlex, Biolin Scientific, Gothenburg, Sweden). All measurements were performed with 10 μ L droplets of Milli-Q water on the surfaces, with contact angle and sliding angle data recorded both parallel and perpendicular to the long axis of the structures.

Sharkskin-like surfaces are known for their distinctive wettability properties. We evaluated the fabricated surfaces for CA, CA hysteresis, and sliding angle to explore these characteristics. We utilized 10 μ L droplets, which are comparable in scale to the structural features, and observed their behavior on the patterned surfaces. The droplets stabilized on the patterned surfaces in specific locations, minimizing contact with higher-height structures. The static contact angle for each droplet was measured 15 s after placement to allow stabilization on the surface. It should be noted that PDMS was used as the substrate material, with tests conducted one week after fabrication. Over time, PDMS surfaces can undergo changes due to the migration of low-molecular-weight species and the adsorption of airborne contaminants. Initially, flat PDMS exhibited a static contact angle of 114.6°. After being stored for five months at room temperature and protected from direct light, the same sample displayed an average static contact angle of 114.1°. This minor variation could be attributed to the aging effects of PDMS or random measurement fluctuations. Notably, the same fabrication method is versatile and can be applied to produce height-varying structures using other moldable polymers tailored to suit specific environmental conditions.

3. Results

3.1. Geometrical Features Characterization

Figure 1a,b displays the SEM images of the PMMA mold and replicated design with PDMS, while Figure 1c,d depicts colorimetric height maps generated by the 3D laser scanning microscope. All fabricated surfaces were characterized to determine their structural heights. The average height of each laser power level was calculated by averaging measurements of average height along the riblet tips of four distinct riblets machined with similar laser parameters. This procedure was applied to all six surfaces to compute their respective structural height levels. Table 1 summarizes the laser parameters and resultant height gradients achieved with the machining process. Height gradient refers to the average inclination of the angled plane that goes through the tips of structures that come into contact with the droplets in contact angle experiments. The deviation from the gradient is calculated as the square root of the sum of the squared differences between each average height level and the gradient plane. This parameter represents the stability of the height variation process.

The penetration depth of the laser is primarily influenced by the laser fluence, which quantifies the energy delivered per unit area. Since the scanning speed was kept constant in our experiments, variations in laser power were used to tune the height. Figure 2a illustrates the average structural height variation with respect to laser power across all fabricated surfaces. The repeatability of each structural height level was characterized by the standard deviation (σ). In Figure 2a, error bars represent the standard deviation of heights at each laser power level, and overall, structural height variation tends to minimize at higher laser powers. Among all the fabricated structures, the heights exhibit a pooled standard deviation of 24.2 μ m, which can be assumed as the tolerance of the process with the equipment used.

3.2. Surface Roughness

To assess surface quality, the profile roughness (R_a) and areal roughness (S_a) of the fabricated structures were measured using surface laser scans. Figure 2b illustrates the variation in average R_a values along the top edge of the structures as a function of laser power. Surface roughness slightly increased with the laser power, consistent with observations in the literature.^[36] The direction of laser scanning significantly influences the measured surface roughness values. Figure 2c shows the surface roughness of the G4 surface, both parallel and perpendicular to the laser scanning direction. A cutoff wavelength (λ_c) of 30 μ m, smaller than any of the designed geometric features, was applied to eliminate surface waviness. The results indicate a higher average surface roughness perpendicular to the scanning direction, likely due to the offset between consecutive laser passes and the residual waviness caused by the greater number of height variations along this axis.

The areal roughness of the riblets was estimated on the G5 surface to capture the complete topography. The average S_a values for riblet areas machined with increasing heights, from the lowest to the highest in equal steps, were 2.4, 3.5, 6.1, 9.2, 12.8, 13.3, 23.3, and 17.7 μ m, respectively, demonstrating a gradual

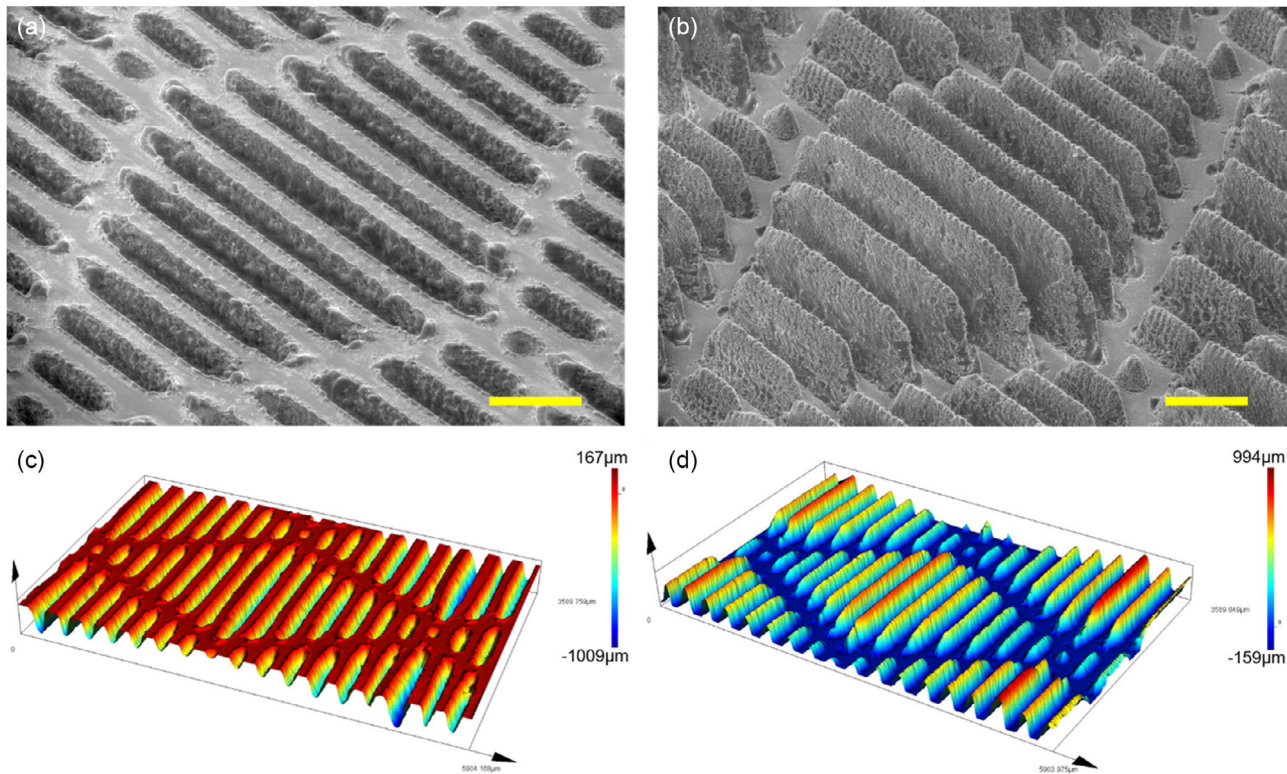


Figure 1. a) SEM image of PMMA mold of G4 surface. The recast layer around the cavities is visible. This resolidified PMMA layer defines the surface quality of the mold. b) Replicated height-varying pattern with PDMS. The scale bars represent 500 μm . c) and d) Color metric height maps of the mold and the replicated design of the G4 surface.

increase with height. This rise in areal roughness is directly associated with the increase in laser power applied across the height gradient. The S_a values reflect only the riblet areas, with a similar cutoff wavelength to that used for surface roughness measurements. Additionally, a periodic waviness pattern with a wavelength of $\approx 50 \mu\text{m}$ was observed along the top edge of each riblet (Figure 2d). This pattern could be attributed to the inherent resolution of the laser machine or mechanical vibrations in the laser system. Figure 2e,f shows the microtexture of the internal surface of the PMMA mold and replicated design. The recast layer, which was formed by the resolidification of molten PMMA, is clearly visible on the PMMA mold. The texture of this layer is copied to the surface of the final PDMS design.

3.3. Theoretical Profile Estimation

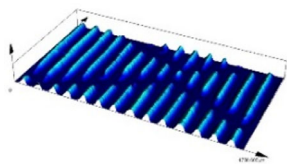
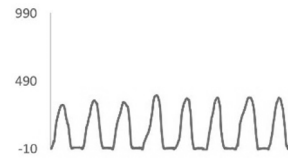
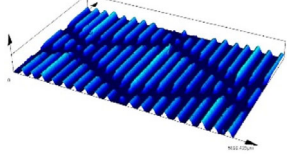
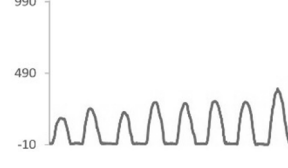
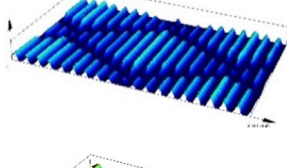
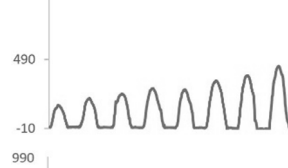
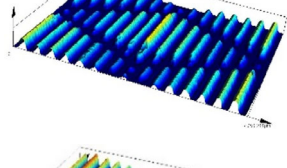
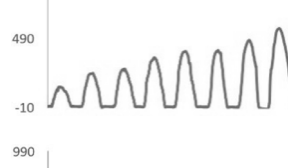
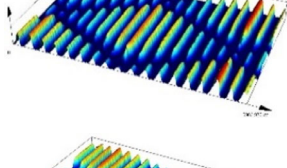
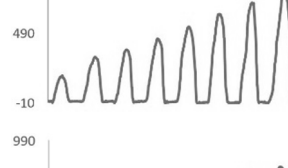
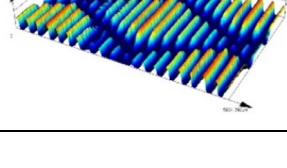
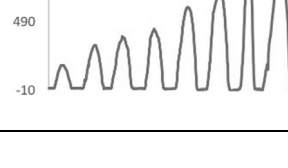
The ablation model described earlier was evaluated against actual machining parameters to assess its accuracy in predicting structural heights. **Figure 3a** compares the theoretical profiles estimated by the model with the experimentally machined profiles of the G5 surface, which features the widest range of laser power variations. The positive replicas were used for this comparison since PDMS can replicate features down to the nanoscale. The design width of the structures was set at 130 μm , with the laser machine software calculating four passes with respective offsets of 30, 20, and 30, which were also used

for theoretical calculations. Experimental absorptivity values for PMMA, as reported by Prakash et al. were used in the model. In the first pass, the laser beam strikes the surface perpendicularly. From the second pass onward, the laser hits the angled surface created by the previous pass, leading to asymmetric machining profiles due to the addition of offsets and changes in absorptivity (Figure 3b). The model's predictions align more closely with higher power levels within our experimental range. The continuous blue line in Figure 2a represents the maximum height of structures estimated by the model over the whole range. The average percentage difference between predicted and actual heights is 25.7% across the entire range. However, for laser powers larger than 7 W, this difference decreases to less than 10%.

3.4. Contact Angle Variation and Theoretical Model Development

The wetting of micropillars with variable height is determined by the behavior of the contact line of a droplet, taking into account the gradient of structural heights. The two classical wetting models, i.e., CB and Wenzel equations, predict the effective CA by considering the solid–liquid interface and the surface roughness factor. However, these models do not account for height variations over a given surface, which adds an extra geometric restriction to droplet spreading and deformation.

Table 1. Geometrical features of the fabricated surfaces and associated laser parameters.

Surface	Laser power and variation (% from 90 W)	3D micrograph (color metric height map) 1000µm -10µm	Cross-sectional height profile (height in µm)	Average height gradient	Deviation from gradient line [µm]
G0	6.2% constant			0.009	10.9
G1	4.6% to 6% in 0.2% steps			0.066	21.5
G2	4.6% to 7.4% in 0.4% steps			0.121	11.0
G3	4.6% to 8.8% in 0.6% steps			0.178	29.7
G4	4.6% to 10.2% in 0.8% steps			0.265	13.9
G5	4.6% to 11.6% in 1% steps			0.298	17.1

To systematically explore the limitations of conventional wetting models, we designed height-variable micropillar structures inspired by the riblets of shark skin. Sharkskin-like riblet patterns are particularly suitable for this study as they provide gradual height variations that would allow for the controlled study of local curvature effects on contact angle formation. With their anisotropic wetting behavior, they serve best for the evaluation of anisotropic discrepancies in classical wetting models, while their structured geometry provides a viable platform to test for the applicability of both the CB and Wenzel equations when applied in nonuniform height conditions. In this way, sharkskin-like riblet patterns can cover fundamental aspects of wettability and assess the theoretical challenges posed by height variations in predicting contact angles.

The measurement conventions are depicted in **Figure 4a**, illustrating the impact of height gradients on droplet alignment. Because of the difference in height structure, the contact line

presents a slanted configuration, causing contact angle and sliding angle changes toward a specific direction. Since the aforementioned anisotropic effect imposes the necessity to reformulate the classical wetting models based on the isotropic roughness or solid fraction distribution assumption, it will thus be necessary to figure quantifications of the deviations. The analysis was further carried out on droplet shapes and the contact angles at different stabilization points, as shown in **Figure 4b**. The figure shows the shapes of 10 µl droplets on each surface at location 1, and **Figure 4c** depicts the variation of contact line angle with the structural height gradient.

3.4.1. Limitations of CB and Wenzel Equations

The angle of the contact plane gradually increases with the structural height gradient. We observed that when viewed parallel to

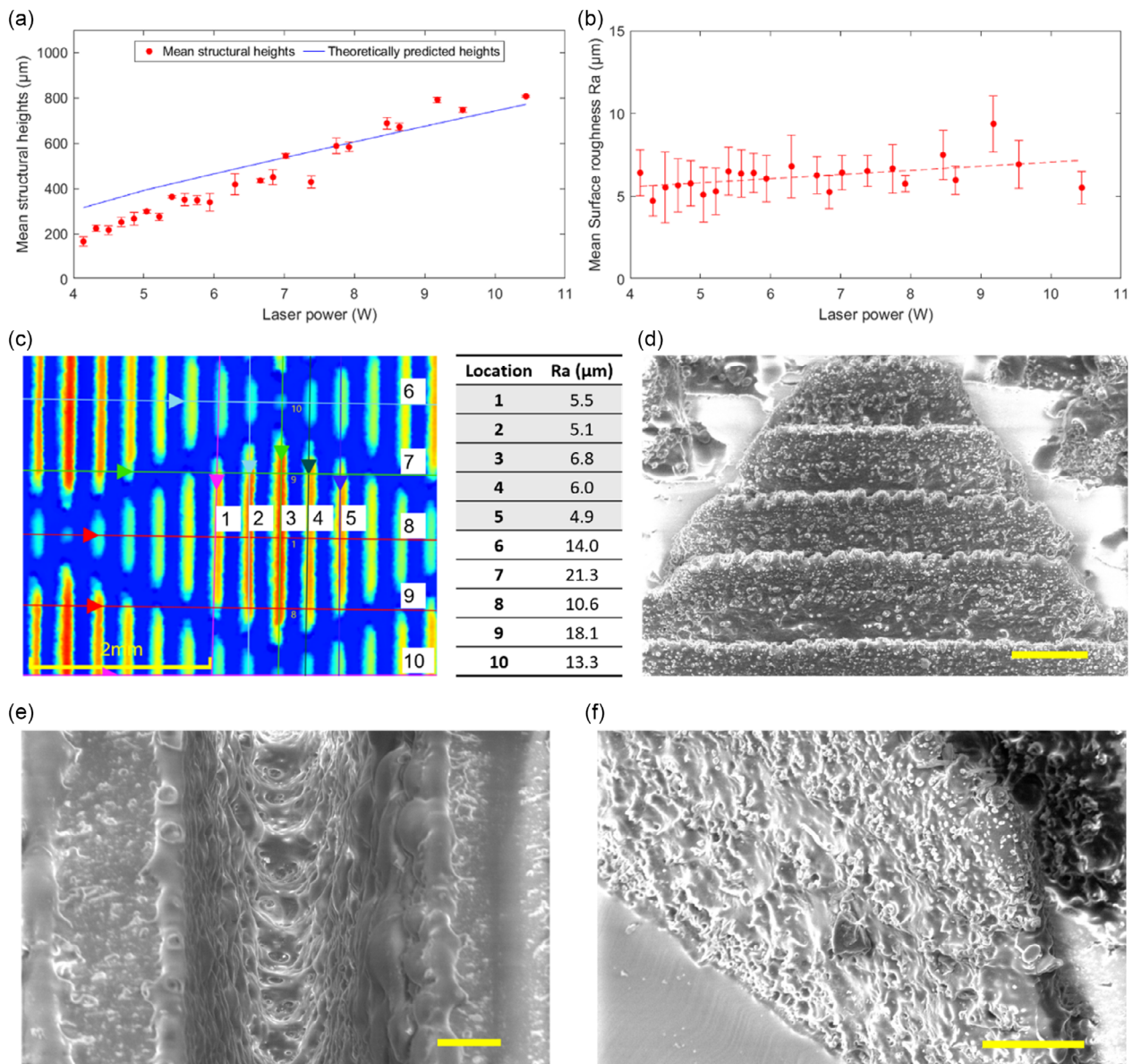


Figure 2. a) Variation of measured mean structural heights and theoretically predicted height with laser power. b) Surface roughness variation with laser power along the laser scanning direction. c) Surface roughness measurement of G4 surface. 1–5 measurements are along the laser scanning direction and 6–10 are perpendicular to the laser scanning direction. d) Observed waviness pattern along the tip of riblets. The scale bar represents 200 μm. e) Internal surface of PMMA mold after laser machining. The scale bar is 50 μm. f) Surface texture of the replicated pattern. The scale bar represents 100 μm. All the error bars represent twice the standard deviation of each data point.

the riblets, droplets consistently remained in a CB state without wetting the side surfaces of the structures. The effective contact angle can be estimated using the CB equation, Equation (2), where the height gradient does not exist.

$$\cos \theta_{\text{effective}} = \sigma_1 (\cos \theta_1 + 1) - 1 \quad (2)$$

where σ_1 represents the solid fraction of the contact area and θ_1 is the contact angle on flat surfaces. However, the model is accurate for predicting the contact angle of structures with uniform heights but does not take into account localized curvatures

due to height variations at the contact line. This is crucial for periodic height-variable micropillars, which cause distinct energy minima for different droplet stabilization levels.

Similarly, when viewed perpendicularly to the riblets (Figure 4a), the droplet wets the microwaviness pattern on the structure's top surface, as mentioned in the surface roughness section. The contact angle from this direction can be theoretically estimated using the Wenzel equation, Equation (3),^[37]

$$\cos \theta_{\text{effective}} = r \cos \theta_1 \quad (3)$$

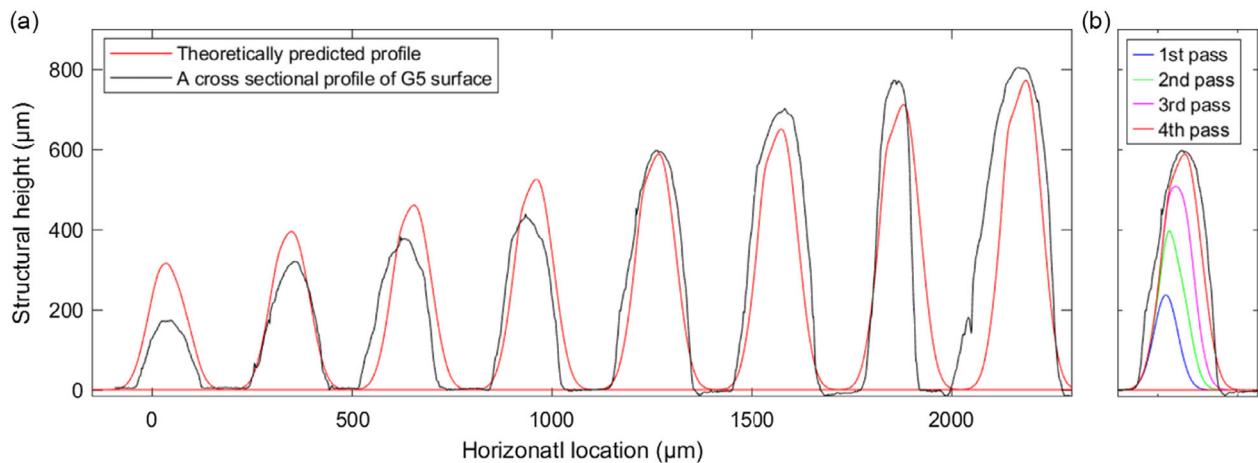


Figure 3. a) Comparison between theoretically predicted and practically machined G5 profiles. b) Theoretically predicted change of profile shape with each laser pass (height level 5 riblet of G5 surface). The asymmetric shape of the practical profile is reflected in the theoretical profile as well.

where r is the roughness factor calculated from the laser microscopy scans along the tip of the riblet, with an average value of 1.37. However, the Wenzel model also assumes a uniform surface roughness, whereas, in reality, height variations create a structured curvature that influences droplet stability.

3.4.2. Height-Gradient Correction in Contact Angle Estimation

3D contact plane geometry and droplet deformation influence the actual contact angle. Overall, the surfaces form a wave pattern, with periodic wells-like geometries formed by the height variation, with the highest points being level 8 riblets and the lowest points being level 4 riblets as the patterns overlap in opposite directions. To better model the influence of height variation, we introduce a correction factor based on the spherical approximation of the droplet's contact plane geometry. This approach, adapted from Wu et al.^[38] assumes that the bottom contact plane of the droplet follows a curved profile rather than a flat surface. The modified equation is as follows

$$V^* = \frac{\sin^3 \theta^*}{\sin^3 \theta} f(\theta) + n \cdot f(\theta^*) \quad (4)$$

where $f(\theta) = (2 - 3 \cos \theta + \cos^3 \theta)/4$, $V^* = 3V_L/(4\pi R^3)$, $\theta^* = \theta' - \theta$. V_L and R are droplet volume and the radius of the bottom surface of the droplet. θ is the new contact angle with the horizontal plane and θ' is the contact angle on a similar surface without height variation. $n = 1$ for the concave surfaces.

This equation introduces an additional correction factor that accounts for the nonuniform contact geometry caused by height variation, leading to improved accuracy in predicting the observed contact angles.

3.4.3. Experimental Validation and Deviation Analysis

Accurate measurement of the top width of the needle-like structures from a side view proved challenging. We approximated the average contact area width as $55.1 \pm 10.1 \mu\text{m}$ based on top views of the droplets, considering the visible contact line and distance

between riblets is $333.9 \pm 0.6 \mu\text{m}$. Although significant intergeometry gaps exist, slight variations in top surface width had a minor effect on the final effective contact angle. Flat PDMS, fabricated using the exact same procedure, exhibited a contact angle of $114.6^\circ \pm 1.3^\circ$. Based on the CB equation, the contact angle for the G0 surface, when viewed parallel to the riblets, was estimated at 155.3° , where the measured average is 143.5° with a maximum value of 150.5° . This difference can be explained by the large contact angle hysteresis reported in the next part.

Figure 4d illustrates the measured variations in contact angles and estimated contact angle with the height gradient of the structures. Static contact angles were measured relative to the angled contact line in surfaces where a height gradient is present. On the G0 surface, the droplet was symmetric. With increasing height gradients, the visible top and bottom contact angles (CA1 and CA2) deviate from each other. Theoretically, estimated values are derived using Equation (4), and the contact angle is calculated using the CB equation for nonheight varying surfaces and the contact line angle to compare them with the measured CA1 values. Estimated CA values show average errors of 5, 9, 8, 9, 1, and 0% compared to measured values in order from lowest to highest height gradient. In surfaces with lower height gradients, droplets could attach to the lower areas between higher patterns, deforming the droplet shape, causing unexpected contact angle changes. The above sharp decrease of error values after 4th pattern could be associated with the detachment of droplets from lower height levels and sitting purely on height variation with a spherical contact plane.

As droplets usually come into contact with more than one riblet, the CB equation can predict the change of contact angle due to discontinuities.^[39] Considering the average solid fraction along the riblet long axis of 0.73, measured from droplet top views, the theoretical CA can be estimated at 135° , which aligns closely with the measured value $139.3^\circ \pm 1.7^\circ$. As height variability increases, the surrounding structures rise, geometrically restricting the droplet and reducing the effective contact angle.

Figure 4e illustrates the practical variation of the contact angle perpendicular (CAP) to the riblets, which consistently decreases

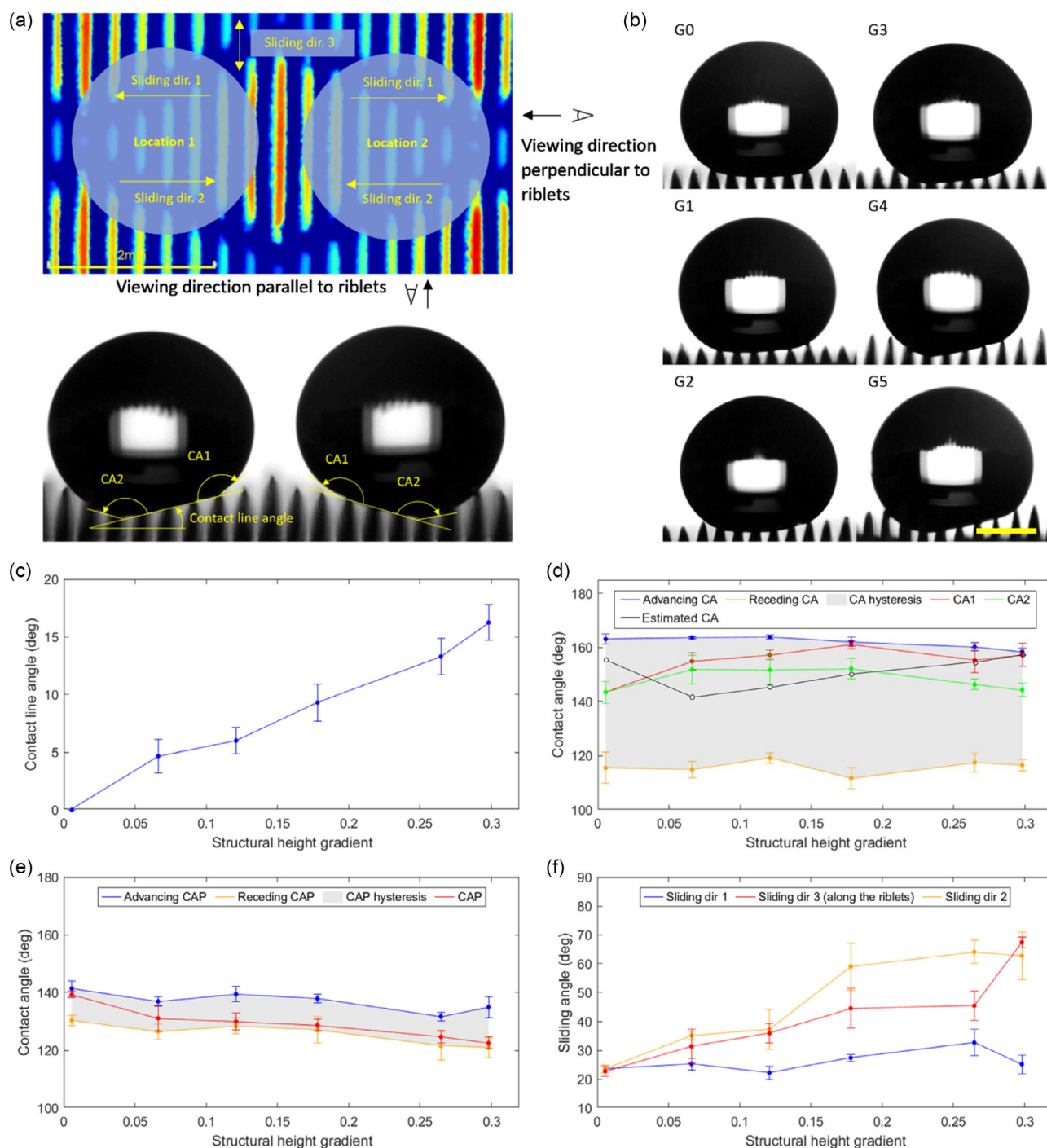


Figure 4. a) Measurement convention of angles, directions, and locational stabilization of droplets on height variable sharkskin patterns. b) Variation of droplet shape with height gradient of the surface. All these droplets are stabilized at location 1 as depicted on the (a). Scale bar represents 1 mm. c) Measured contact line angle changes with the structural height gradient. d) Variation of 10 µl droplet contact angles against the height gradient on fabricated sharkskin surfaces viewed parallel to riblets. The black color line represents the theoretically estimated contact angle using Equation (4). e) Variation of 10 µl droplet contact angles on fabricated sharkskin surfaces viewed perpendicular to the riblets. f) Variation of droplet sliding angles with structural height gradient (length of all the error bars equal to two times the standard deviation of each data point).

with the height gradient. According to the literature, Equation (4) can also be used, combined with the Wenzel equation for non-planar surfaces. However, correction with Equation (4) in the

perpendicular direction yields increasing CA values with increasing height gradient, which contradicts the results. This could be associated with the convex shape of the contact plane viewed

perpendicular to the riblets by droplet pinning on low-height riblets at the edges.

Dynamic contact angles (advancing and receding) were measured from both parallel and perpendicular viewing directions to the riblets to more accurately quantify the surface properties by inflating and deflating the sessile drop. Due to the large interriblet gaps on these surfaces, the contact line jumps between geometries as the droplet volume changes.

Viewed parallel to the riblets, as the droplet initially shows different contact angles based on the location (CA1 and CA2), the droplet continually advances in the direction with a lower contact angle. Due to surface geometry, the contact line shows a wavy behavior over the droplet, and all angles were measured relative to the local contact line. The measured average advancing angle slightly decreases with the height gradient, while the receding angle shows no evident variation (Figure 4d).

Generally, the stable contact angle can take any value between the advancing and receding angles based on the droplet placement method and geometrical restrictions. Droplets were placed on the surface using the tensiometer's built-in pipette, which moves down and deposits the droplet on the surface. Inconsistencies in the droplet placement process due to surface height variations and large contact angle hysteresis could have caused the significant variations of CA1 and CA2 values depicted as the error bars in Figure 4d. Relatively lower contact angle hysteresis in the perpendicular viewing direction to the riblets explains the more stable variation of the CAP values in Figure 4e.

The sliding angle of the droplet directly depends on the advancing and receding contact angles. The following Equation (5) gives the relationship between dynamic contact angles (θ_r , θ_a) and sliding angle (θ_{sliding}) on a flat surface according to the force balance.^[40]

$$\sin \theta_{\text{sliding}} = \frac{w\gamma_L k}{mg} (\cos \theta_r - \cos \theta_a) \quad (5)$$

where w , γ_L , and mg are the width of the contact area, the surface tension of the water, and the droplet's weight, respectively. " k " is a constant that depends on the droplet shape, which is the predominant factor that alters the sliding angle in this situation. Generally, for flat surfaces, k can be approximated as 1. Sliding directions 1, 2, and 3 of droplets are selected as depicted in Figure 4a.

On the G0 surface, without a height gradient, the average maximum riblet contact width is estimated to be $1,066 \pm 42 \mu\text{m}$ from the droplet images captured perpendicular to the riblets. Considering $k = 1$, for $10 \mu\text{L}$ droplets sliding in any direction on the G0 surface, the sliding angle can be calculated as 24.4° , which is comparable with the practically measured value of $23.6^\circ \pm 2.3^\circ$. For other surfaces with height gradients, the contact area length (w) increases with the height gradient, which causes an increase in the sliding angle in both directions 1 and 2. The geometrical inclination of the contact plane added to the sliding angle in direction 2, while it has an adverse effect on the sliding angle in direction 1. However, the increasing structural heights impose geometrical constraints that restrict sliding in direction 1, resulting in a lack of clear, practical variation as a cumulative effect of these factors. Figure 4f shows the variation of sliding angles with structural heights. The sliding angle in direction 2 kept increasing as no negative factors were affecting it.

Considering sliding direction 3, along the riblets, the contact area width shows significantly smaller values as the droplet contacts only with 4 or 5 riblets depending on the droplet placement conditions. With a measured average contact area width of $55.1 \pm 10.1 \mu\text{m}$ per riblet, Equation (4) estimates a sliding angle of less than 5° for measured dynamic contact angles for G0 surface, which is significantly smaller than the practically measured value of $22.8^\circ \pm 3.2^\circ$. When viewed perpendicularly to the riblets, the surface exhibits large continuous geometries, resulting in reduced contact angle hysteresis, as shown in Figure 4e. However, practically, once the droplet moves slightly, it gets attached to the edges of riblets, causing a significant increase in dynamic contact angles and force required for depinning, increasing the sliding angle. In G1 to G5 surfaces, variable height structures pose a geometrical restriction on sliding, further increasing the sliding angles.

Usually, surfaces with high contact angles are associated with low sliding angles, which make droplets slide off the surface easily. On these surfaces, fluid contact shows hydrophobic properties with large contact angles only wetting the tip of droplets. Droplets in two directions (directions 2 and 3) show increasing sliding angles with height gradient while sliding in direction 1 remains primarily stable. The rose petal effect is a similar phenomenon that shows large contact angles with high adhesion induced by the hierarchical structures on the surfaces. These surfaces show similar properties in specific directions, making them both anisotropic and unidirectional for droplet sliding.

As a final note, it is worth mentioning that micro- and nano-scale surface modifications are among the most critical factors in enhancing surface-based sensing or catalytic performance.^[41] Microscale surface modifications, such as micropillars, significantly increase the effective surface area and improve the interaction of analytes with the surface.^[42–44] When there is a flow on the surface, height-varying structures can induce more chaotic flow behavior, thereby enhancing mass transfer to the surface. As such, the height-varying micropillars could have essential applications in improving biosensing efficiency or catalytic performance.

4. Conclusion

This study demonstrated the feasibility of using direct laser machining with varying laser fluence to fabricate height-variable microstructures for soft lithography applications. Compared to traditional methods, this approach simplifies fabrication, reduces costs, and accelerates processing. The fabricated structures exhibited consistent height variability and demonstrated hydrophobic properties, with anisotropic wettability effects influenced by structural orientation. These findings suggest potential applications in droplet manipulation, surface flow control, and sample storage.

Beyond fabrication, we systematically investigated the limitations of classical wetting models (CB and Wenzel equations) when applied to height-variable microstructures. Experimental results revealed that traditional models fail to fully capture the effect of height gradients on droplet behavior, necessitating a modified theoretical framework. By introducing a corrected equation incorporating height-dependent contact plane curvature, we improved the predictive accuracy of wettability on structured surfaces. Our findings provide a refined theoretical

framework for wetting mechanics on nonuniform microstructured surfaces.

The proposed fabrication method can also be extended to create height-varying microstructures such as micropillars, which can be leveraged for biosensing and surface fluid manipulation. Future work will explore the integration of these structures in biosensing platforms, focusing on their ability to enhance mass transfer and analyte interaction. Additionally, computational modeling and further experimental validation will refine the modified wetting model, validating its applicability for diverse microfluidic and engineered surface applications.

Acknowledgements

This work was performed in part at the Queensland node of the Australian National Fabrication Facility (ANFF). A company established under the National Collaborative Research Infrastructure Strategy (NCRIS) to provide nano- and microfabrication facilities for Australia's researchers.

Open access publishing facilitated by Griffith University, as part of the Wiley - Griffith University agreement via the Council of Australian University Librarians.

Conflict of Interest

The authors declare no conflict of interest.

Author Contributions

Prabuddha De Saram: data curation (lead); investigation (equal); methodology (equal); software (lead); validation (equal); visualization (lead); writing—original draft (lead); writing—review editing (equal). **Nam-Trung Nguyen:** formal analysis (equal); funding acquisition (equal); project administration (equal); supervision (equal); writing—review editing (equal). **Navid Kashaninejad:** conceptualization (lead); formal analysis (equal); funding acquisition (lead); investigation (equal); methodology (lead); project administration (lead); resources (lead); supervision (lead); validation (equal); writing—review editing (lead).

Data Availability Statement

The data that support the findings of this study are available from the corresponding author upon reasonable request.

Keywords

anisotropic wettability, laser micromachining, sharkskin-like surfaces, variable-height microstructures

Received: January 23, 2025

Revised: February 22, 2025

Published online:

- [1] D. Qin, Y. Xia, G. M. Whitesides, *Nat. Protoc.* **2010**, *5*, 491.
- [2] M. A. Rose, J. J. Bowen, S. A. Morin, *ChemPhysChem* **2019**, *20*, 909.
- [3] S. Razavi Bazaz, N. Kashaninejad, S. Azadi, K. Patel, M. Asadnia, D. Jin, M. Ebrahimi Warkiani, *Adv. Mater. Technol.* **2019**, *4*, 1900425.
- [4] D. Barata, E. Provaggi, C. van Blitterswijk, P. Habibovic, *Lab Chip* **2017**, *17*, 4134.
- [5] Z. Isiksacan, M. T. Guler, B. Aydogdu, I. Bilican, C. Elbuken, *J. Micromech. Microeng.* **2016**, *26*, 035008.

- [6] J. Li, W. Tan, W. Xiao, R. P. Carney, Y. Men, Y. Li, G. Quon, Y. Ajena, K. S. Lam, T. Pan, *Anal. Chem.* **2018**, *90*, 13969.
- [7] S. Vidya, R. Wattal, L. Singh, P. Mathiyalagan, *CO₂ Laser Micromachining Of Polymethyl Methacrylate (PMMA): A Review*, Springer Nature Singapore, Singapore **2021**, pp. 939–945.
- [8] S. Prakash, S. Kumar, in *Microfabrication and Precision Engineering* (Ed: J. Paulo Davim), Woodhead Publishing **2017**, pp. 163–187.
- [9] G. Srikantaprasad, N. Tom Mathew, *Mater. Today: Proc.* **2023**, *102*, 432.
- [10] A. B. Sözmen, A. Arslan Yildiz, *Microfluid. Nanofluid.* **2021**, *25*, 66.
- [11] H. Klank, J. Kutter, P. O. Geschke, *Lab Chip* **2002**, *2*, 242.
- [12] Z. Yan, X. Huang, C. Yang, *Microfluid. Nanofluid.* **2017**, *21*, 1.
- [13] J. Wei, J. Shi, B. Wang, Y. Tang, X. Tu, E. Roy, B. Ladoux, Y. Chen, *Microelectron. Eng.* **2016**, *158*, 22.
- [14] X. Cui, D. Chen, H. Chen, *ACS Omega* **2023**, *8*, 8569.
- [15] X. Zhang, Y. Liu, C. Yao, J. Niu, H. Li, C. Xie, *Nanoscale Adv.* **2023**, *5*, 142.
- [16] R. K. Annavarapu, S. Kim, M. Wang, A. J. Hart, H. Sojoudi, *Sci. Rep.* **2019**, *9*, 405.
- [17] A. Saez, M. Ghibaudo, A. Buguin, P. Silberzan, B. Ladoux, *Proc. Natl. Acad. Sci. U.S.A.* **2007**, *104*, 8281.
- [18] S. O'Halloran, A. Pandit, A. Heise, A. Kellett, *Adv. Sci.* **2023**, *10*, e2204072.
- [19] A. Jaiswal, C. K. Rastogi, S. Rani, G. P. Singh, S. Saxena, S. Shukla, *iScience* **2023**, *26*, 106374.
- [20] A. Ghimire, R. B. Dahl, S. F. Shen, P. Y. Chen, *Adv. Funct. Mater.* **2024**, *34*, 2307121.
- [21] Y. W. Park, T. W. Kim, *Mater. Res. Innovations* **2014**, *18*, S2-992.
- [22] Y. C. Jung, B. Bhushan, *J. Phys. Condens. Matter.* **2010**, *22*, 035104.
- [23] G. D. Bixler, B. Bhushan, *J. Colloid Interface Sci.* **2013**, *393*, 384.
- [24] G. D. Bixler, B. Bhushan, *Adv. Funct. Mater.* **2013**, *23*, 4507.
- [25] B. Dean, B. Bhushan, *Philos. Trans. A Math. Phys. Eng. Sci.* **2010**, *368*, 4775.
- [26] S. Martin, B. Bhushan, *J. Colloid Interface Sci.* **2016**, *474*, 206.
- [27] H. R. Holmes, K. F. Böhringer, *Microsyst. Nanoeng.* **2015**, *1*, 1.
- [28] D. G. Gagnon, D. Park, K. Yim, S. Morozova, *Soft Matter* **2024**, *20*, 4079.
- [29] M. S. Ambrosia, M. Y. Ha, S. Balachandar, *Appl. Surf. Sci.* **2013**, *282*, 211.
- [30] A. G. Domel, G. Domel, J. C. Weaver, M. Saadat, K. Bertoldi, G. V. Lauder, *Bioinspir. Biomim.* **2018**, *13*, 056014.
- [31] J. Huang, Q. Wang, Z. Wu, Z. Ma, C. Yan, Y. Shi, B. Su, *Adv. Funct. Mater.* **2021**, *31*, 2103776.
- [32] A. F. H. Kaplan, *J. Appl. Phys.* **1996**, *79*, 2198.
- [33] N. B. Dahotre, S. P. Harimkar, *Laser Fabrication and Machining of Materials*, Springer New York, New York, NY, USA **2007**.
- [34] S. Prakash, S. Kumar, *J. Micromech. Microeng.* **2015**, *25*, 035010.
- [35] S. Prakash, S. Kumar, *Precis. Eng.* **2017**, *49*, 220.
- [36] K. Ninikas, J. Kechagias, K. Salonitis, *J. Manuf. Mater. Process.* **2021**, *5*, 74.
- [37] A. Hongru, L. Xiangqin, S. Shuyan, Z. Ying, L. Tianqing, *RSC Adv.* **2017**, *7*, 7052.
- [38] D. Wu, P. Wang, P. Wu, Q. Yang, F. Liu, Y. Han, F. Xu, L. Wang, *Chem. Phys.* **2015**, *457*, 63.
- [39] A. Marmur, *Langmuir* **2003**, *19*, 8343.
- [40] H.-J. Butt, J. Liu, K. Koynov, B. Straub, C. Hinduja, I. Roismann, R. Berger, X. Li, D. Vollmer, W. Steffen, M. Kappl, *Curr. Opin. Colloid Interface Sci.* **2022**, *59*, 101574.
- [41] Y. Liu, W. Zhang, *Nat. Catal.* **2023**, *6*, 985.
- [42] S. Numthuam, T. Ginoza, M. Zhu, H. Suzuki, J. Fukuda, *Analyst* **2011**, *136*, 456.
- [43] M. Geissler, A. Ponton, C. Nassif, L. Malic, K. Turcotte, L. Lukic, K. J. Morton, T. Veres, *ACS Appl. Polym. Mater.* **2022**, *4*, 5287.
- [44] M. Zhou, D. Gao, Z. Yang, C. Zhou, Y. Tan, W. Wang, Y. Jiang, *Talanta* **2021**, *222*, 121480.